Volume 21 | Number 33 | 7 September 2019 | Pages 4831–5004

CrystEngComm

rsc.li/crystengcomm

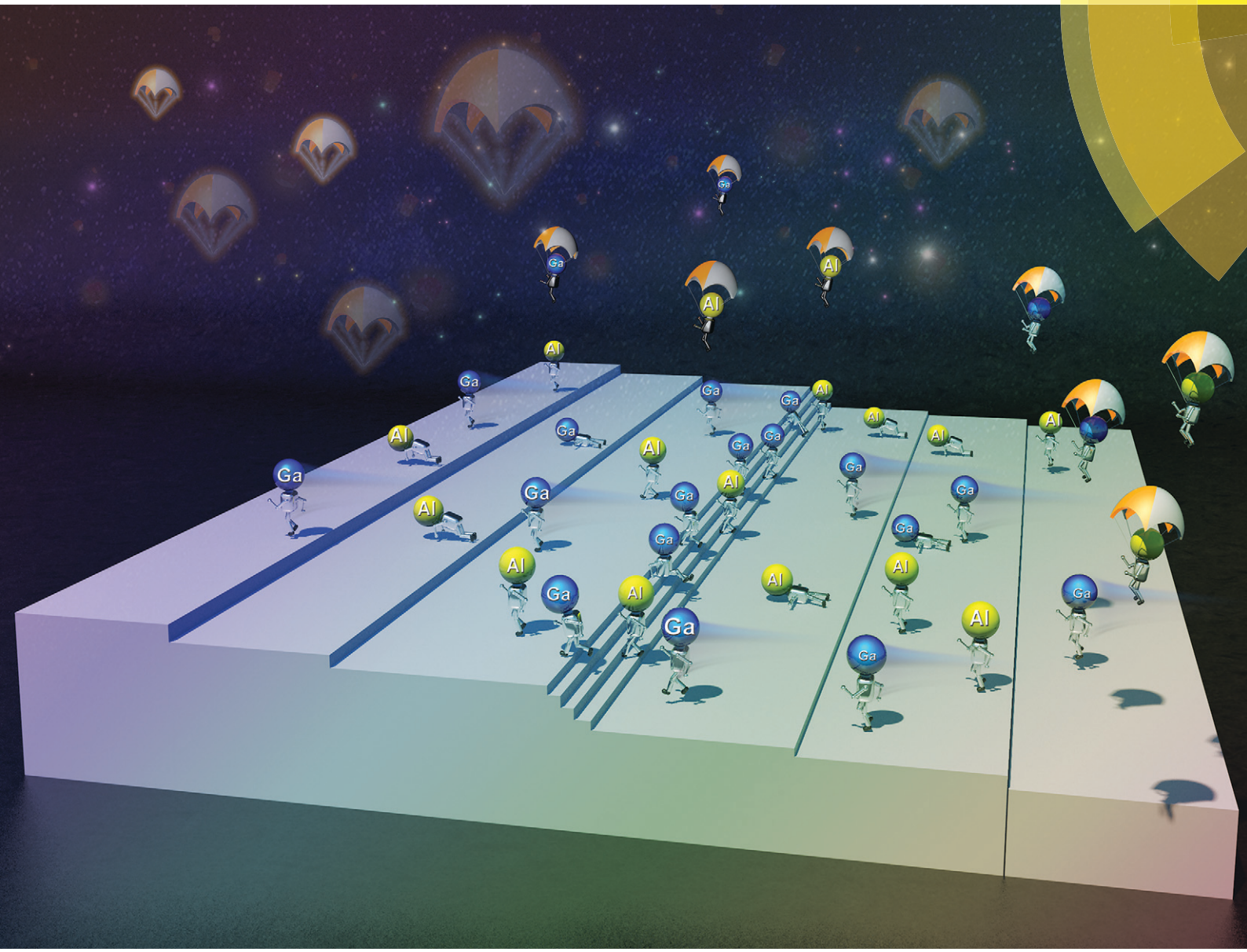

ISSN 1466-8033

ROYAL SOCIETY OF CHEMISTRY | Celebrating IYPT 2019

PAPER
Xiaojuan Sun *et al.*
Suppressing the compositional non-uniformity of AlGaN grown on a HVPE-AlN template with large macro-steps

CrystEngComm

PAPER

View Article Online
View Journal | View Issue

Cite this: *CrystEngComm*, 2019, **21**, 4864

Suppressing the compositional non-uniformity of AlGaN grown on a HVPE-AlN template with large macro-steps

Ke Jiang,[ab] Xiaojuan Sun, *[ab] Jianwei Ben,[ab] Zhiming Shi,[ab] Yuping Jia,[ab] You Wu,[ab] Cuihong Kai,[ab] Yong Wang[ab] and Dabing Li [ab]

AlGaN is a promising material for ultraviolet optoelectronic and microelectronic devices. In this report, we investigated the influences of metallization pretreatment on the strain, morphology and optical properties of AlGaN grown on HVPE-AlN. The results indicated that the pretreatment could effectively alleviate the compressive strain from HVPE-AlN and thus lower the Al-content in AlGaN. The composition pulling effect was considered to be responsible for the Al-content reduction. On the other hand, the pretreatment could help to improve the surface morphology of AlGaN, which was attributed to the growth mode transition involved in the pretreatment. Besides, the optical measurements revealed that the AlGaN directly grown on HVPE-AlN exhibited distinct compositional non-uniformity and the reasons were the macro-steps in the surface of HVPE-AlN and the mobility discrepancy of Al and Ga atoms. The pretreatment could eliminate such non-uniformity effectively. The carbon clusters formed by metal–organic decomposition during the pretreatment were believed to be responsible for the improvement. The localized excitonic characteristics were also studied. It was found that the localized excitonic states were abundant and energy transport processes were complex in AlGaN directly grown on HVPE-AlN, which would result in undesired light emissions. The pretreatment was proved to be effective in optimizing the localized excitonic characteristics, which may be attributed to the alleviation of Al-content fluctuation by the pretreatment. These results can not only provide a deeper understanding of AlGaN epitaxy, but also offer an approach to optimize the properties of the AlGaN materials.

Received 23rd April 2019,
Accepted 18th June 2019

DOI: 10.1039/c9ce00608g

rsc.li/crystengcomm

Introduction

The growth of AlGaN has received extensive attention due to its promising applications in deep-ultraviolet (DUV) optoelectronic devices and high-power electronic devices. Because of its direct and tunable wide-band gap, the working wavelength of AlGaN-based optoelectronic devices covers the region from DUV of 200 nm to near UV of 365 nm. AlGaN is thus the ideal material for solar-blind photodetectors (PDs), UV light-emitting diodes (LEDs), and laser diodes (LDs). Moreover, AlGaN is also suitable for metal-oxide-semiconductor field effect transistors (MOSFETs) and high electron mobility transistors (HEMTs).[1–5] However, the growth of high-quality AlGaN is extremely difficult compared to that of GaN owing to the weak surface migration of Al atoms. Otherwise, the commercial GaN substrates cannot assist the growth of AlGaN since tensile stress associated cracks usually exist on the AlGaN layer on the GaN substrate.

AlN substrates are the best substrates for AlGaN growth due to their compressive stress on the upper AlGaN layers. However, the growth of AlGaN has mainly been performed on AlN buffer layers nucleated on lattice-mismatched sapphire substrates due to the limitation of commercially available AlN substrates to date. So, many methods have been applied to improve the quality of AlN templates and thus the subsequent AlGaN materials, such as a two-step growth method,[6] low temperature (LT) or middle temperature (MT) interlayer method,[7,8] and epitaxial lateral overgrowth (ELOG) method.[9–11] Still, the quality of AlN buffer layers is unsatisfactory. Recently, a clear and DUV transparent AlN/sapphire template with a mirror-like surface obtained by hydride vapor phase epitaxy (HVPE) has become commercially available, which opens a new way to develop AlN and Al-rich AlGaN by homoepitaxy. AlN homoepitaxy based on HVPE has been studied before,[12] while the AlGaN epitaxy based on HVPE still remains to be investigated until now.

Although HVPE-AlN is usually more than 5 μm, the strain cannot be completely released due to the large mismatch

[a] *State Key Laboratory of Luminescence and Applications, Changchun Institute of Optics, Fine Mechanics and Physics, Chinese Academy of Sciences, Changchun 130033, China. E-mail: sunxj@ciomp.ac.cn*
[b] *Center of Materials Science and Optoelectronics Engineering, University of Chinese Academy of Sciences, Beijing 100049, China*

between the AlN template and the sapphire substrate. Such remaining strain will consequently affect the upper AlGaN layer, especially the metal atom incorporation.[13–15] Therefore, how to alleviate the influences of the sapphire substrate on the upper AlGaN layer is also a valuable research issue. On the other hand, the kink sites are indispensable for AlN growth on foreign substrates such as sapphire because the surface adsorbed atoms need positions to incorporate and then to nucleate. The method to acquire kink sites is usually to cut the substrate along the vicinal face of the growth face. Moreover, the cutoff was demonstrated to have a positive effect on dislocation reduction and stress management.[16–18] To attain better quality thick AlN templates, the cutoff angle toward the *a*-plane or *m*-plane can usually range from 0.1° to 6°.[16,19] However, there are also disadvantages with the cutoff in sapphire. The cutoff may result in poor surface or interface smoothness in heterostructures because the bunching effect may happen and macro-steps will be generated.[19–22] And the macro-steps will result in compositional non-uniformity and further deteriorate the light emission properties in the subsequent epilayers.[16,19,20] So it is necessary to investigate the influences of HVPE-AlN on the upper grown AlGaN layer and to find an approach to eliminate the harmful effects.

Metallization pretreatment is commonly used in the growth of III-nitrides to improve the material surface morphology.[23–26] It can suppress the formation of SiN_x when silicon is used as a substrate,[25,26] and it can suppress the formation of N-polarity materials when sapphire is used as a substrate.[23,24,27–29] However, whether the metallization pretreatment has effects on epitaxial AlGaN grown on HVPE-AlN still remains unclear. Based on previous research studies,[23–29] it can be expected that the metallization pretreatment would have positive effects on the AlGaN epitaxy on HVPE-AlN.

In this report, we investigated the influences of metallization pretreatment on the strain, morphology and optical properties of epitaxial AlGaN grown on HVPE-AlN. To reveal the influences, AlGaN epilayers were directly grown on commercial HVPE-AlN by high-temperature metal–organic chemical vapor deposition (HT-MOCVD). Then trimethylaluminum (TMAl) and trimethylgallium (TMGa) mixed flow pretreatment of the HVPE-AlN was introduced. The results implied that the compressive stress could be released and the surface morphology could be improved by the pretreatment. Otherwise, the pretreatment could also alleviate the compositional non-uniformity and alloy potential fluctuation, thus suppressing the undesired light emissions and optimizing localized excitonic characteristics. The investigation presented here will make a significant step in understanding the growth of epitaxial AlGaN on the HVPE-AlN and thus obtaining high quality AlGaN materials and devices.

Experimental

The AlGaN epilayers were grown using an AIX200/4 RF-S THMOCVD system. TMAl, TMGa and ammonia (NH_3) were used as Al, Ga and N precursors, and hydrogen (H_2) was used as the carrier gas, respectively. The substrates were commercial 2 inch 5–6 μm thick HVPE-AlN/sapphire templates with a sapphire cutoff angle of about 1.5 ± 0.2° toward the *a*-plane, which are provided by Suzhou Nanowin Science and Technology Co., Ltd (NANOWIN). During the AlGaN growth procedure, the chamber pressure and total flow rate were fixed at 40 mbar and 9600 sccm, respectively. AlGaN layers were grown directly on HVPE-AlN at 1180 °C without and with metallization pretreatment, which are denoted as samples A and B, respectively. The flow rates of TMAl, TMGa and NH_3 were 40 sccm, 12 sccm and 500 sccm. To pretreat the HVPE-AlN templates, the NH_3 flow was closed for 20 s while the TMAl and TMGa flows were kept at 40 sccm and 12 sccm. The total growth times of the AlGaN epilayers were both 40 minutes.

X-ray diffraction reciprocal space mapping (RSM) was used to analyze the strain and composition profile. The equipment is a Bruker D8 Discover thin film diffractometer. The X-ray source is a Cu $K_{\alpha1}$ radiation line with a wavelength of 0.15406 nm. *In situ* curvature and reflection monitoring curves were extracted to study the strain and surface roughness evolution during the growth. Then atomic force microscopy (AFM, Bruker Multimode 8) was used to observe the surface morphology. At the same time, cathodoluminescence measurements (CL) were used to study the light emission properties at different positions over the AlGaN epilayers. The working voltage ranged from 4 kV to 20 kV and the electronic beam current was kept at 6.2 nA. The integration time and the scanning step were 0.1 s and 0.1 nm, respectively. Moreover, temperature dependence photoluminescence measurements (PL) were applied to analyze the optical properties of AlGaN epilayers. The excitation wavelength of the femtosecond laser is 217 nm and the output power is 20 mW. The repetition frequency of the light pulse is 76 MHz. During the measurements, the integration time was kept at 0.2 s and the scanning step was 0.5 nm. The temperature dependence PL measurements were carried out at temperatures varying from 10 K to 300 K.

Results and discussion

The RSM measurements were employed to analyse the strain and composition profile. Fig. 1(a) and (b) show the (10–14) asymmetric plane RSMs of samples A and B, respectively. The inserts in each graph are the corresponding epitaxial structure schematic diagrams. The thickness of HVPE-AlN is more than 5 μm and those of HT-MOCVD AlGaN epilayers are about 1.1 μm and 1.2 μm. The upper reciprocal lattice points (RLPs) belong to HVPE-AlN substrates and the lower ones belong to AlGaN epilayers. It is shown that the center of the AlGaN RLP of sample A almost aligns with the line of R = 0 which is called the 'completely strained line', implying the strong compressive stress in the AlGaN epilayer caused by HVPE-AlN. In contrast, the center of the AlGaN RLP of sample B is located quite close to the line of R = 1 which is called the 'completely relaxed line', indicating the low stress in the AlGaN epilayer caused by HVPE-AlN. Otherwise, the RLP

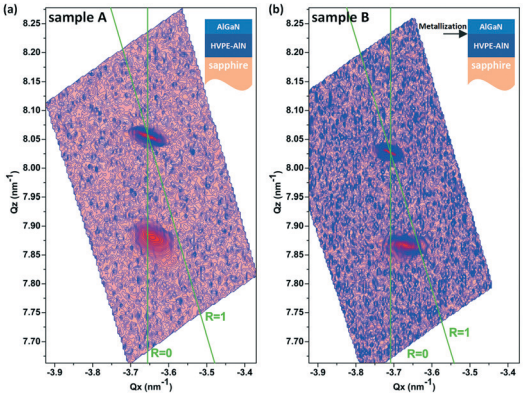

Fig. 1 The (10–14) asymmetric plane RSMs of (a) sample A and (b) sample B, respectively. The inserts in (a) and (b) are the epitaxial structure schematic diagrams of samples A and B, respectively.

discrepancy may also originate from the limited lateral size and composition difference.[30] From the RSMs, the lattice constants can be determined by formula (1),

$$\begin{cases} a = 2\sqrt{\dfrac{h^2 + h\cdot k + k^2}{3Q_x^{\,2}}} \\ c = \dfrac{l}{Q_z} \end{cases} \tag{1}$$

where (Q_x, Q_z) is the RLP center of the (hkl) planes. The center position coordinates of the AlN and AlGaN RLPs of samples A and B are (−3.6508, 8.0543), (−3.7094, 8.0272), (−3.6413, 7.8809), and (−3.6716, 7.8669), respectively. Based on formula (1) and asymmetry (10–14) plane RSM results, the AlGaN lattice constants a and c of samples A and B can be ascertained, respectively.

It is reasonable to assume that the III-nitrides satisfy the biaxial-stress conditions due to their hexagonal structures. Therefore, the lattice constants of the AlGaN layer obey the following equation, eqn (2),[31]

$$\frac{c(x) - c_0(x)}{c_0(x)} = -2\cdot\frac{C_{13}(x)}{C_{33}(x)}\cdot\frac{a(x) - a_0(x)}{a_0(x)} \tag{2}$$

where $c(x)$ and $a(x)$ stand for the measured out-of-plane and in-plane lattice constants of the $Al_xGa_{1-x}N$ layer, $c_0(x)$ and $a_0(x)$ stand for the out-of-plane and in-plane lattice constants of the strain-free $Al_xGa_{1-x}N$ layer, and $C_{13}(x)$ and $C_{33}(x)$ are the elastic constants of the $Al_xGa_{1-x}N$ layer, respectively. As for the strain-free $Al_xGa_{1-x}N$, the lattice constants can be obtained from Vegard's law as formula (3),[32]

$$\begin{cases} a_0(x) = a_0^{\mathrm{AlN}}\cdot x + a_0^{\mathrm{GaN}}\cdot(1-x) \\ c_0(x) = c_0^{\mathrm{AlN}}\cdot x + c_0^{\mathrm{GaN}}\cdot(1-x) \end{cases} \tag{3}$$

where a_0^{AlN}, c_0^{AlN}, a_0^{GaN} and c_0^{GaN} are the lattice constants of strain-free AlN and GaN, respectively. By applying a linear interpolation method as shown in formula (4),

$$\begin{cases} C_{13}(x) = C_{13}^{\mathrm{AlN}}\cdot x + C_{13}^{\mathrm{GaN}}\cdot(1-x) \\ C_{33}(x) = C_{33}^{\mathrm{AlN}}\cdot x + C_{33}^{\mathrm{GaN}}\cdot(1-x) \end{cases} \tag{4}$$

where C_{13}^{AlN}, C_{33}^{AlN}, C_{13}^{GaN}, and C_{33}^{GaN} are the elastic constants of AlN and GaN whose values are taken to be 108 GPa, 373 GPa, 103 GPa, and 405 GPa,[33] respectively, the elastic constants $C_{13}(x)$ and $C_{33}(x)$ of $Al_xGa_{1-x}N$ layers can be obtained. Eventually, a cubic equation for Al content x can be derived from eqn (2)–(4). Through solving the cubic equation, the Al content x and relaxation R of the AlGaN epilayer of samples A and B can be determined to be 61% and 0.14 and 51% and 0.89, respectively, which quantitatively verified the different strain states between the AlGaN epilayers of samples A and B.

To further investigate the strain variation during the growth procedure, the *in situ* temperature and curvature monitoring curves of samples A and B were obtained as shown in Fig. 2(a) and (b), respectively. At the very beginning, the curvatures of samples A and B are almost the same. However, during the AlGaN growth procedure, the curvature of sample A gradually decreases while that of sample B almost stays constant. It is worth noting that the curvature of sample A varied from a positive value to a negative value, implying that the stress exerted on the AlGaN epilayer changed from tensile stress to compressive stress. Meanwhile, the AlGaN epilayer in sample B continually suffered from tensile stress. At the end of the growth, sample A exhibits a much larger curvature value than sample B, indicating that the AlGaN layer in sample A suffered from stronger compressive stress than that in sample B, which was demonstrated by the RSM results. This difference distinctly reflects that the interaction

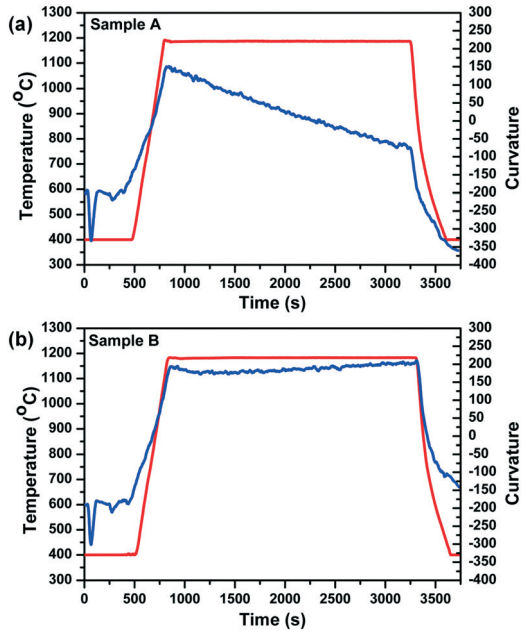

Fig. 2 The *in situ* temperature and curvature monitoring curves of (a) sample A and (b) sample B. The red curves are for temperature and the blue curves are for curvature.

between the epilayer and substrate of sample A is stronger than that of sample B. Except for the metallization pretreatment, the growth conditions for samples A and B were completely the same. Thus it can be concluded that it was the metallization pretreatment that released the compressive stress from HVPE-AlN.

On the other hand, such an obvious difference in composition deserves to be investigated. It has been demonstrated that the inherent strain state will affect the composition profile, which is called the 'composition pulling effect'.[13–15] In AlGaN alloys, the Ga atoms will be expelled out when they are under compressive stress while the Al atoms will be expelled out when they are under tensile stress to lower the system total strain energy.[3,34] The above analysis confirmed that the AlGaN epilayer in sample A suffered from stronger compressive stress than that in sample B. Besides, the metal element enrichment during the pretreatment cannot directly reduce the Al-content. So it can be deduced that the composition difference was from the strain pulling effect. From the perspective of energy, the strain energy density of a multilayer system can be estimated by the following equation, formula (5),[35]

$$E_s = 2 \cdot G \cdot \frac{1+\nu}{1-\nu} \cdot \sum d_i \cdot \varepsilon_i^2 \quad (5)$$

where E_s is the strain energy density, G and ν are the Shear modulus and Poisson's ratio, and d_i and ε_i are the thickness and strain value of each layer. Previous research illustrated that the elastic modulus of AlGaN with different Al contents had a similar value of about 375 GPa.[36] Besides, the Poisson's ratio of AlN and GaN are 0.203 and 0.183, respectively, from which the AlGaN epilayers of samples A and B can take the value of 0.193.[33,37] The calculated strain energy density values of samples A and B are 5.945×10^5 J m^{-2} and 1.758×10^5 J m^{-2}, respectively. Therefore, the conclusion that metallization pretreatment can lower the Al-content in the AlGaN epilayer as well as the total strain energy density by releasing the compressive stress from HVPE-AlN can be drawn.

The surface morphology evolution was analyzed by AFM as shown in Fig. 3. Fig. 3(a) is the AFM image of HVPE-AlN within the scale of 10 μm × 10 μm. There are many large macro-steps originating from the large cutoff angle in the sapphire substrate.[12,17,18] The HT and low V/III ratio make the Al atoms energetic enough to overcome the Ehrlich–Schwoebel barrier and thus the bunching effect will happen when AlN templates are grown by HVPE. Eventually, the macro-steps will arise on the surface as shown in Fig. 3(a). When AlGaN layers were directly grown on such HVPE-AlN as sample A, the macro-steps still existed on the surface and the step width became much wider than the substrate, as shown in Fig. 3(b). Besides, the surface of sample A became much rougher as it can be seen from the scale bar on the side. However, the introduction of metallization pretreatment to the HVPE-AlN could release such phenomena. As shown in Fig. 3(c), sample B exhibits a much narrower step width than sample A and even the HVPE-AlN. From the results, it can be deduced that the bunching effect may continue to work and to deteriorate the surface morphology when directly growing AlGaN on HVPE-AlN while the pretreatment can alleviate the influences. But the mechanisms leading to such differences need further investigation.

The CL measurements were carried out at electronic acceleration voltages of 4 kV, 5 kV, 10 kV, 15 kV and 20 kV with an electronic beam current of 6.2 nA at different positions of samples A and B. The resulting spectra within one sample show similar characteristics but those belonging to different samples are quite different. Fig. 4 shows the typical CL spectra of samples A and B. As for sample B, there is only one emission peak located at 4.485 eV, which coincides with the Al content determined from the RSM results. The slight asymmetry at the low energy side of the spectrum was attributed to the band tail states. However, a broader emission spectrum was obtained from sample A as shown in Fig. 4. Two peaks located at 4.471 eV and 4.677 eV can be observed by applying the Gaussian function to fit the spectrum. There is no doubt that the higher energy emission of 4.677 eV originated from the intrinsic radiation of sample A. But the origin of the lower energy emission of 4.471 eV remains unclear. In

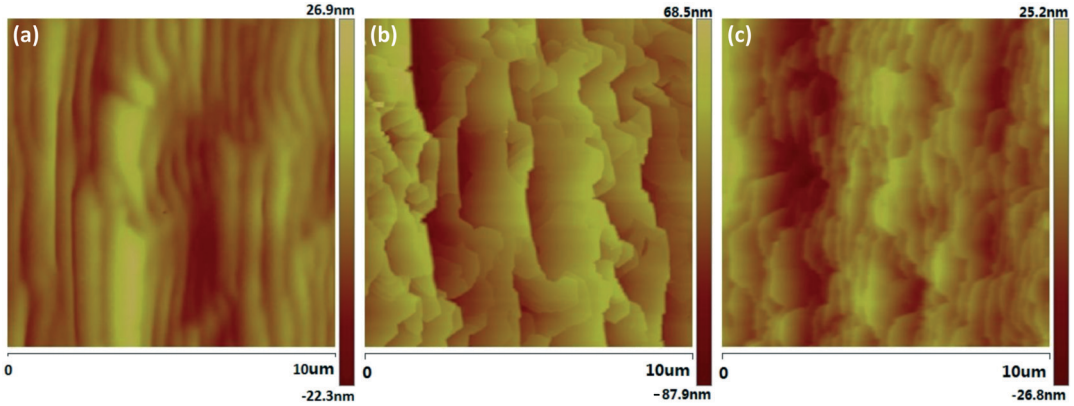

Fig. 3 The AFM images of (a) HVPE-AlN substrates, (b) sample A and (c) sample B with a scale of 10 μm × 10 μm.

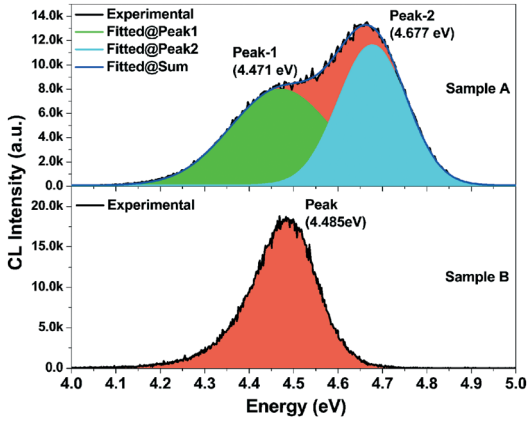

Fig. 4 The CL spectra of samples A and B measured at an electronic acceleration voltage of 5 kV and an electronic beam current of 6.2 nA. The black curves are the experimental results and the colored ones are the fitted curves.

previous reports, such light emission abnormality was observed and it was attributed to compositional non-uniformity.[16,19,20] In the RSM results, it can also be seen that the AlGaN RLP of sample A is not symmetrical, and the tailing of the RLP points to the low Al direction, indicating the compositional non-uniformity in sample A. However, whether the compositional non-uniformity in sample A is along the vertical or horizontal direction remains unclear and further studies need to be done.

Different electronic acceleration voltages correspond to different penetration depths. The energy distribution and maximum energy depth at different electronic acceleration voltages can be calculated by applying H. J. Fitting's electronic energy density distribution law as formula (6),[38]

$$\frac{dE}{dx} = C_1 \cdot E^{0.3} \cdot \left\{ \exp\left[-B \cdot \left(\frac{x - x_0}{R(E)} \right)^2 \right] + k_1 \cdot \exp\left(-k_2 \cdot \left| \frac{x - x_k}{R(E)} \right| \right) \right\} \quad (6)$$

where x is the depth in nm, E is the electronic acceleration voltage in keV, and C_1, B, $x_0/R(E)$, k_1, k_2 and $x_k/R(E)$ are all empirical constants related to the average atomic number of the material. $R(E)$ is the maximum penetration depth of electrons at the acceleration voltage E in nm estimated by the K–O equation (7),[39]

$$R(E) = 27.6 \cdot \frac{\bar{A}}{\rho \cdot \bar{Z}^{\frac{8}{9}}} \cdot E^{\frac{5}{3}} \quad (7)$$

where ρ is the material density in g cm^{-3}, and $\bar{A}$ and $\bar{Z}$ are the average atomic weight and number, respectively. The average atomic weight and number of AlGaN with Al content x were obtained by a linear interpolation method. The needed empirical constants were determined by the atomic number of $Al_xGa_{1-x}N$ through linearly fitting the constants with atomic numbers provided by H. J. Fitting.[38]

Fig. 5(a) shows the normalized energy distributions of $Al_{0.6}Ga_{0.4}N$ at electronic acceleration voltages of 4 kV, 5 kV, 10 kV, 15 kV and 20 kV, respectively. The electron energy density gradually increases with increasing penetration length and reaches a maximum at a certain depth. Then the electron energy density will fleetly decrease to zero. The variation of the maximum energy density depth and the maximum penetration depth in AlGaN with Al content at the electronic acceleration voltages of 4 kV, 5 kV, 10 kV, 15 kV and 20 kV were calculated as shown in Fig. 5(b) and (c). The maximum energy density depth and maximum penetration depth increase with the rise of the Al content and the electronic acceleration voltages. At electronic acceleration voltages of 4 kV and 5 kV, the electron beam energy concentrates on the position about 100 nm beneath the surface and then vanishes at 200 nm. When the electronic acceleration voltage rises to 10 kV, 15 kV and 20 kV, the electron beam energy concentrates on the positions about 200–300 nm, 400–600 nm, and 600–1000 nm beneath the surface, respectively. Correspondingly, the electron beam energy vanishes within about 400–700 nm, 1.0–1.5 μm, and 1.5–2 μm. So the CL spectra at different electronic acceleration voltages can reflect the information at different depths.

As for samples A and B whose Al contents are 0.61 and 0.51, the depths of maximum energy density at electronic acceleration voltages of 4 kV, 5 kV, 10 kV, 15 kV, and 20 kV are 56 nm, 80 nm, 253 nm, 496 nm, and 801 nm, and 53 nm, 76 nm, 240 nm, 472 nm, and 761 nm, respectively. Since the AlGaN epilayers are about 1.2 μm, it can be confirmed that the CL signals mainly came from the corresponding depths of the AlGaN epilayer. The resulting spectra at different electronic acceleration voltages of one sample showed a similar behavior to that shown in Fig. 4. However, for sample A, as the electronic acceleration voltage and the position alter, the peak positions of the lower and higher energy peaks show no notable changes as Fig. 5(d) and (e) show, which demonstrates that the above-mentioned compositional non-uniformity is along the horizontal direction. Further, the CL panchromatic images of sample A also confirmed the horizontal compositional non-uniformity. On the other aspect, it was found that the CL intensity ratio of low energy to high energy emission peaks gradually increased as the electronic acceleration voltage increased as shown in Fig. 5(f). At an identical voltage, the ratio only oscillates slightly at different positions. The voltage dependent CL measurements were also applied to sample B, and it was found that the wavelength fluctuation between 4 kV and 20 kV at different positions was within 50 meV. This phenomenon implies that the compositional non-uniformity was severest at the beginning of the directly grown AlGaN on HVPE-AlN. As the AlGaN thickness increased, the compositional non-uniformity gradually became relatively mild. Therefore, it can be concluded that horizontal compositional non-uniformity would happen and such non-uniformity would gradually relax as the thickness

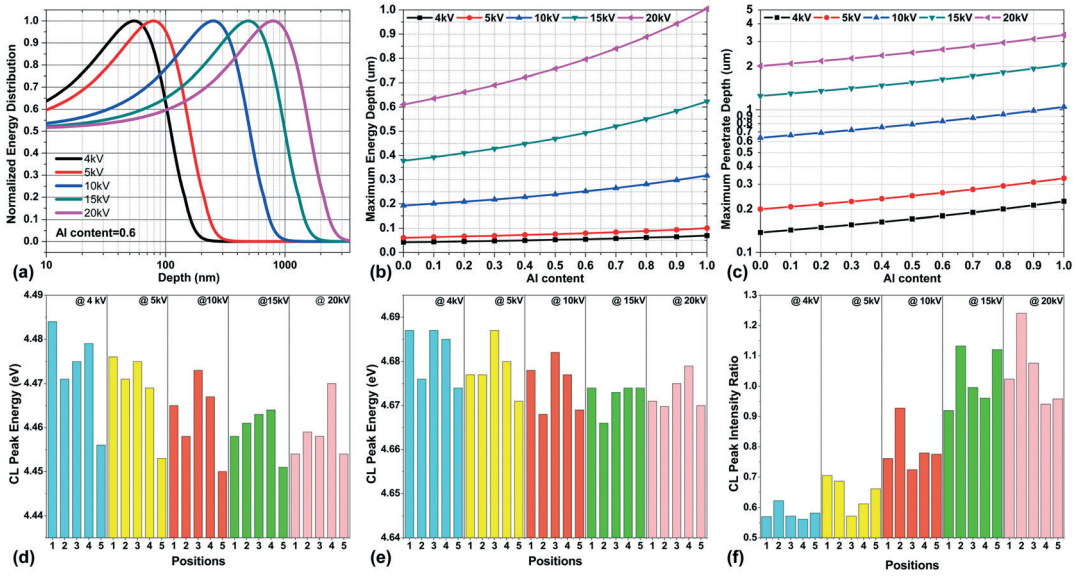

Fig. 5 (a) is the calculated normalized electronic energy distributions in $Al_{0.6}Ga_{0.4}N$ at different electronic acceleration voltages. (b) and (c) are the calculated maximum energy depth and maximum penetration depth in AlGaN with different Al contents at different electronic acceleration voltages. (d) and (e) are the peaks of sample A at different electronic acceleration voltages and positions for the lower and higher energy peaks, respectively. (f) is the CL peak intensity ratio of the lower to higher energy peaks of sample A at different electronic acceleration voltages.

increased when AlGaN was directly grown on HVPE-AlN. And the metallization pretreatment could effectively suppress the compositional non-uniformity. However, the mechanisms of the horizontal compositional non-uniformity generation and relaxation with increasing thickness, as well as the suppression by the metallization pretreatment, all remain to be studied.

As it can be seen in Fig. 3(a), many macro-steps exist in the surface of HVPE-AlN. When growing AlGaN layers directly on such substrates, the bunching effect might continue to work. However, the introduction of Ga atoms in the AlGaN growth would lengthen the migration distance of metal atoms. And a HT of 1180 °C would also favor the atom migration especially Ga atoms. Consequently, the step width might further expand and some macro-steps might vanish with increasing thickness, which can be clearly observed in Fig. 3(b). On the other hand, the Al atoms migrate slower than the Ga atoms and the Al atoms also have a shorter migration

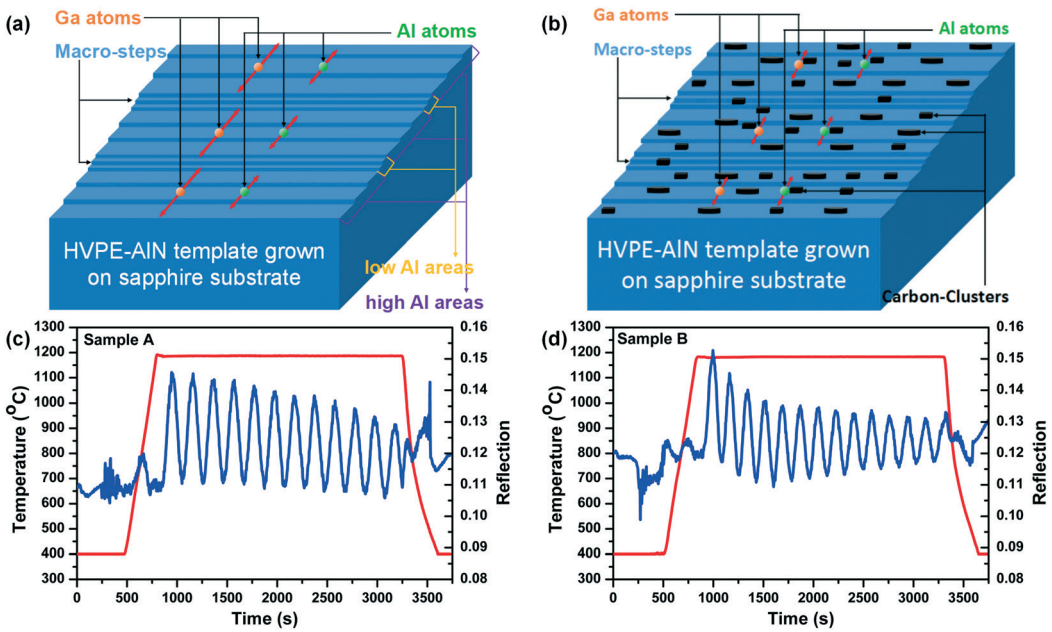

Fig. 6 (a) is the schematic diagram of the formation mechanism of compositional non-uniformity. (b) is the mechanism schematic diagram of the metallization pretreatment preventing the compositional non-uniformity. (c) and (d) are the reflection curves for samples A and B, respectively.

distance than the Ga atoms at a certain temperature. Potentially, the Al atoms might not have enough energy to cross the Ehrlich–Schwoebel barrier, while the Ga atoms could overcome the Ehrlich–Schwoebel barrier and stop at the macro-step areas or even cross a macro-step area to another, as shown in Fig. 6(a). Eventually, the macro-step areas contained a higher Ga content than other areas. The *in situ* reflection monitoring curve, as shown in Fig. 6(c), continues to decrease during the AlGaN growth, which supports the above analysis. As for sample B, the surface morphology was improved and the compositional non-uniformity was suppressed by the metallization pretreatment. Once the so-called 'two-monolayer mode' was used to explain the phenomena. However, if the metal atomic monolayers were formed, the metal atoms would migrate further at the beginning of the AlGaN growth, resulting in a much broader step width. So it can be deduced that there might be some other mechanisms. In recent research studies, it was found that the metal–organics would decompose to form carbon clusters when pretreating the substrates using metal–organics.[28,29] So the mechanisms of metallization pretreatment improving the surface morphology and eliminating the compositional non-uniformity can be explained in Fig. 6(b). Due to the absence of an NH_3 flow at the very beginning of the AlGaN growth, the metal–organic flows would decompose to form randomly distributed carbon clusters on the HVPE-AlN, which could effectively impede the metallic atoms to migrate. So the Ga atoms could not migrate further than Al atoms and thus the compositional non-uniformity was suppressed. Moreover, during the growth of AlGaN, the carbon clusters could play the role of masks. The AlGaN epilayer would prefer the three-dimensional (3D) growth mode at the beginning. As the thickness increased, the 3D islands coalesced and the growth mode transitioned to a two-dimensional (2D) growth mode. Therefore, the bunching effect would be alleviated and the surface morphology would be improved. Fig. 6(d) shows the *in situ* reflection monitoring curve of sample B. As the growth proceeded, the reflection curve decreased first and then increased, which supports the 3D growth mode transition to the 2D growth mode.

The influences of the metallization pretreatment on the optical properties of AlGaN grown on HVPE-AlN were then investigated. Fig. 7(a)–(c) show the normalized temperature dependence PL spectra at temperatures ranging from 10 K to 300 K, the PL spectrum at 10 K and the PL spectrum at 300 K of sample A, respectively. There are two main emission peaks for the AlGaN epilayer both at 10 K and 300 K, as shown in Fig. 7(b) and (c), which are similar to the CL spectra, confirming the existence of compositional non-uniformity. When applying the Gaussian function to fit the PL spectra at 10 K and 300 K, at least four Gaussian curves are essential, indicating that there may be complex defects. According to the peak intervals, the defects can be deduced as shallow donor defects.[40,41] With increasing temperature, as shown in Fig. 7(a), the peak positions at each temperature present a slight shift and the shift does not possess the typical S-shape

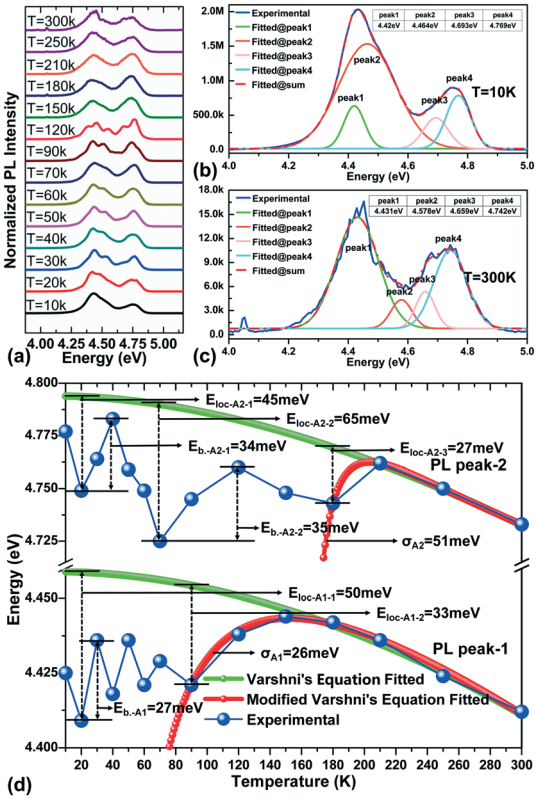

Fig. 7 (a) is the normalized temperature dependence PL spectra from 10 K to 300 K for sample A. (b) and (c) are the PL spectra of sample A at 10 K and 300 K, respectively. (d) is the PL peak positions at different temperatures for sample A.

as the PL spectra of AlGaN alloys usually present. At certain temperatures such as 30 K, 90 K and 120 K, some more peaks appear in the PL spectra. The peak positions at different temperatures were extracted from the PL spectra and plotted in Fig. 7(d). The upper blue curve is the dependence of higher energy peak positions on the temperature. As temperature increases, three minima appear at 20 K, 70 K and 180 K, which indicates that there may be three types of localized exciton states. Varshni's equation was applied to estimate the localized excitonic energy (E_{loc}) which is defined as the difference between the theoretical band-gap and the minimum.[42] Theoretically, the band-gap will reduce with temperature as Varshni's equation (8),[42]

$$E_g(T) = E_g(0) - \frac{\alpha T^2}{\beta + T} \quad (8)$$

where $E_g(T)$ and $E_g(0)$ are the band-gap at temperature of T (K) and 0 K, and α and β are Varshni's coefficients, respectively. By fitting the band-gap at temperature higher than 180 K, the theoretical band-gaps can be obtained as the upper green curve. Accordingly, the localized exciton energies at 20 K, 70 K and 180 K, which are denoted as $E_{loc\text{-}A2\text{-}1}$, $E_{loc\text{-}A2\text{-}2}$, and $E_{loc\text{-}A2\text{-}3}$, are 45 meV, 65 meV and 27 meV, respectively.

Different localized excitons played the main role at different temperatures, indicating the carrier transport among localized excitons. The carrier transport barrier ($E_{barrier}$) can also be estimated as the difference between the maxima and minima. The $E_{barrier}$ values from localized exciton states $E_{loc\text{-}A2\text{-}1}$ to $E_{loc\text{-}A2\text{-}2}$ and $E_{loc\text{-}A2\text{-}2}$ to $E_{loc\text{-}A2\text{-}3}$, which are denoted as $E_{barrier\text{-}A2\text{-}1}$ and $E_{barrier\text{-}A2\text{-}2}$, are 34 meV and 35 meV. The exciton localization is always attributed to the random alloy potential fluctuation, which results in the typical S-shaped temperature dependence band-gap curve.[42–44] The random alloy potential fluctuation can be estimated from modified Varshni's equation (9),[45]

$$E_g(T) = E_g(0) - \frac{\alpha T}{\beta + T} - \frac{\sigma^2}{k_B T} \quad (9)$$

where k_B is the Boltzmann constant and σ is the standard deviation in the case of the most probable Gaussian distribution of the potential fluctuation. The upper red curve in Fig. 7(d) is the fitted band-gap using eqn (9), resulting in a σ_{A2} value of 51 meV, which implies a large potential fluctuation. The lower blue, green and red curves in Fig. 7(d) are the temperature dependent PL peak positions of the lower energy side of sample A and theoretical fitting curves by Varshni's equation at temperature higher than 120 K and modified Varshni's equation at temperature higher than 70 K, respectively. At temperatures of 20 K and 90 K, two minima exist and the corresponding E_{loc} values can be determined to be $E_{loc\text{-}A1\text{-}1}$ = 50 meV and $E_{loc\text{-}A1\text{-}2}$ = 33 meV, respectively. The carrier transport barrier $E_{barrier\text{-}A1}$ from localized exciton states $E_{loc\text{-}A1\text{-}1}$ to $E_{loc\text{-}A1\text{-}2}$ is 27 meV. It is noticeable that peak position vibration exists between 20 K and 90 K, indicating that defect energy levels may play an important role in the carrier transport from a localized exciton state to another. In addition, the potential fluctuation σ_{A1} is calculated to be 26 meV.

As for sample B, the results are different. Fig. 8(a)–(c) show the normalized temperature dependence PL spectra at temperatures ranging from 10 K to 300 K, the PL spectrum at 10 K and the PL spectrum at 300 K of sample B, respectively. Only one main emission peak exists with a narrower spectral width both at 10 K and 300 K as shown in Fig. 8(b) and (c). When using the Gaussian function to fit the PL spectrum at 10 K, there are three peaks located at 4.441 eV, 4.522 eV and 4.596 eV, respectively. The two lower energy peaks were first speculated to be LO phonon replicas. However, the LO phonon energies of GaN and AlN are 91 meV and 110 meV,[46,47] which implies that the emissions are not LO phonon replicas. So it is believed that there are still shallow donor defects in the AlGaN epilayer of sample B. However, the shallow donor defect types in the AlGaN epilayer of sample B are less than that in sample A. The variation of peak positions of sample B with temperatures exhibits more ordinary and affirmatory, as shown in Fig. 8(a). The peak positions at different temperatures were extracted from the PL spectra and plotted in Fig. 8(d). With increasing temperature, the peak position first

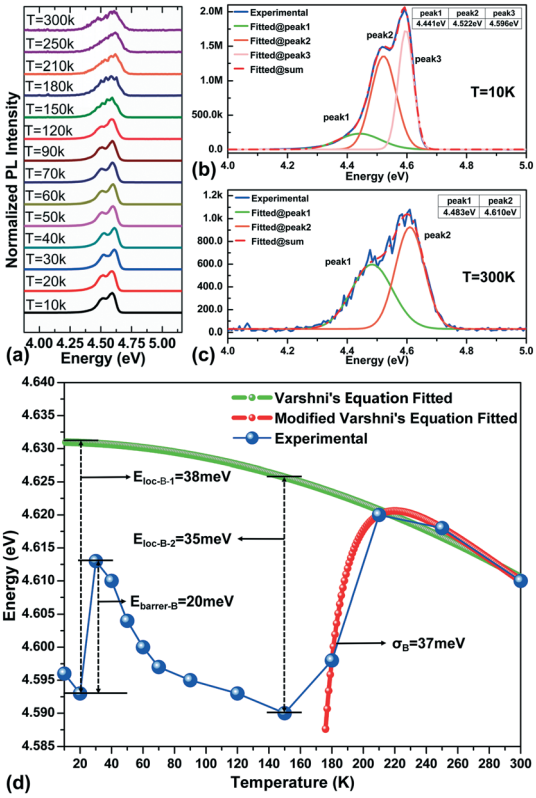

Fig. 8 (a) is the normalized temperature dependence PL spectra from 10 K to 300 K for sample B. (b) and (c) are the PL spectra of sample B at 10 K and 300 K, respectively. (d) is the PL peak positions at different temperatures for sample B.

red-shifts and then blue-shifts. When the temperature increases to higher than 40 K, a typical S-shape curve is obtained. The green and red curves are theoretical fitting curves by Varshni's equation and modified Varshni's equation at different temperatures, respectively. Two localized exciton states are obtained with an $E_{loc\text{-}B\text{-}1}$ value of 38 meV and an $E_{loc\text{-}B\text{-}2}$ value of 35 meV and the carrier transport barrier $E_{barrier\text{-}B}$ is 20 meV. Besides, the potential fluctuation σ_B is 37 meV.

Based on the calculations of localized excitonic energies, carrier transport barriers and alloy potential fluctuations, it can be known that there are abundant localized exciton states with high localization energy and the carrier transport barriers are high in the higher Al content areas of sample A. This is due to the high alloy potential fluctuation. Besides, as the carriers transport in the lower Al content areas of sample A, some defect levels will participate. These localized excitonic characteristics will complicate the carrier transport and the light emission. However, for the metallization pretreated sample B, there are only two localized exciton states and the localized exciton energies are very close. In addition, the carrier transport barrier is comparatively smaller than that of sample A. This can be attributed to the lower alloy potential fluctuation. Conclusively, the metallization pretreatment can be used to suppress the redundant excitonic states, to

alleviate the discrepancy between localized excitons and thus to improve the light emission properties.

Conclusions

In summary, the influences of metallization pretreatment on AlGaN homoepitaxy by HT-MOCVD on HVPE-AlN have been investigated. It was found that the metallization pretreatment could release the compressive stress to the AlGaN epilayer from HVPE-AlN. The Al content will be lowered due to the pulling effect. The surface morphology can also be improved by the metallization pretreatment, which can be explained by the growth mode transition from 3D to 2D. The macro-steps in the surface of HVPE-AlN would result in detrimental composition non-uniformity. The mobility discrepancy between Al and Ga atoms and the obstructive effect of the macro-steps on Ga atoms were responsible for the non-uniformity. The metallization pretreatment could effectively suppress the non-uniformity as the metal–organics would decompose to form carbon clusters that would diminish the mobility discrepancy between Al and Ga atoms. Otherwise, the AlGaN directly grown on HVPE-AlN would have abundant localized exciton states and complex energy transport processes, which would result in undesired light emissions. The metallization pretreatment could suppress redundant excitonic states, alleviate the discrepancy between excitons and thus optimize the light emission characteristics. These results indicate that the metallization pretreatment is an approach available to optimize the properties of epitaxial AlGaN and then to improve the performances of DUV optoelectronic devices.

Conflicts of interest

There are no conflicts to declare.

Acknowledgements

This work was supported by the National Key R&D Program of China [2016YFB0400101], the National Science Fund for Distinguished Young Scholars [61725403], the National Natural Science Foundation of China [61874118, 61574142, 61322406, and 61827813], the Key Program of the International Partnership Program of CAS [181722KYSB20160015], the Special Project for Inter-government Collaboration of the State Key Research and Development Program [2016YFE0118400], the Science and Technology Service Network Initiative of the Chinese Academy of Science, Jilin Provincial Science & Technology Department [20150519001JH], the CAS Interdisciplinary Innovation Team, and the Youth Innovation Promotion Association of CAS [2015171].

References

1 T. Yoshitaka, M. Kasu and T. Makimoto, *Nature*, 2006, **441**(7091), 325–328.
2 H. Yoshida, T. Yamashita, M. Kuwabara and H. Kan, *Appl. Phys. Lett.*, 2008, **93**(24), 241106.
3 Y. K. Dong, P. H. Jun, W. L. Jong, S. Y. Hwang, S. J. Oh, J. Kim, C. Sone, E. F. Schubert and J. K. Kim, *Light: Sci. Appl.*, 2015, **4**(4), e263.
4 L. Dabing, S. Xiaojuan, S. Hang, L. Zhiming, C. Yiren, J. Hong and M. Guoqing, *Adv. Mater.*, 2012, **24**(6), 845–849.
5 L. Dabing, J. Ke, S. Xiaojuan and G. Chunlei, *Adv. Opt. Photonics*, 2018, **10**(1), 43–110.
6 S. Xiaojuan, L. Dabing, C. Yiren, S. Hang, J. Hong, L. Zhiming, M. Guoqing and Z. Zhiwei, *CrystEngComm*, 2013, **15**(30), 6066–6073.
7 L. Xiaohang, W. Shun, X. Hongen, O. W. Yong, K. Tsung-Ting, S. Md. Mahbub, S. Shyh-Chiang, Y. Paul Douglas, D. Theeradetch, R. D. Dupuis, A. M. Fischer and F. A. Ponce, *Phys. Status Solidi B*, 2015, **252**(5), 1089–1095.
8 M. Nakarmi, B. Cai, J. Y. Lin and H. X. Jiang, *Phys. Status Solidi A*, 2012, **209**(1), 126–129.
9 M. Kim, T. Fujita, S. Fukahori, T. Inazu, C. Pernot, Y. Nagasawa, A. Hirano, M. Ippommatsu, M. Iwaya, T. Takeuchi, S. Kamiyama, M. Yamaguchi, Y. Honda, H. Amano and I. Akasaki, *Appl. Phys. Express*, 2011, **4**, 092102.
10 M. Imura, K. Nakano, T. Kitano, N. Fujimoto, G. Narita, N. Okada, K. Balakrishnan, M. Iwaya, S. Kamiyama, H. Amano, I. Akasaki, K. Shimono, T. Noro, T. Takagi and A. Bandoh, *Appl. Phys. Lett.*, 2006, **89**(22), 221901.
11 Z. Lisheng, X. Fujun, W. Jiaming, H. Chenguang, G. Weiwei, W. Mingxing, S. Bowen, L. Lin, Q. Zhixin, W. Xinqiang and S. Bo, *Sci. Rep.*, 2016, **6**, 35934.
12 J. Ke, S. Xiaojuan, B. Jianwei, J. Yuping, L. Henan, W. Yong, W. You, K. Cuihong and L. Dabing, *CrystEngComm*, 2018, **20**(19), 2720–2728.
13 S. Pereira, M. R. Correia, E. Pereira, K. P. O'donnell, C. Trager-Cowan, F. Sweeney and E. Alves, *Phys. Rev. B: Condens. Matter Mater. Phys.*, 2001, **64**(20), 205311.
14 Y. L. Tsai, C. L. Wang, P. H. Lin, W. T. Liao and J. R. Gong, *Appl. Phys. Lett.*, 2003, **82**(1), 31–33.
15 B. Liu, R. Zhang, J. G. Zheng, X. L. Ji, D. Y. Fu, Z. L. Xie, D. J. Chen, P. Chen, R. L. Jiang and Y. D. Zheng, *Appl. Phys. Lett.*, 2011, **98**(26), 261916.
16 I. Bryan, Z. Bryan, S. Mita, A. Rice, L. Hussey, C. Shelton, J. Tweedie, J. P. Maria, R. Collazo and Z. Sitar, *J. Cryst. Growth*, 2016, **451**, 65–71.
17 X. Q. Shen, H. Matsuhata and H. Okumura, *Appl. Phys. Lett.*, 2005, **86**(2), 021912.
18 X. Q. Shen, M. Shimizu and H. Okumura, *Jpn. J. Appl. Phys.*, 2003, **42**(11A), L1293.
19 H. Mengjun, Q. Zhixin, Z. Lisheng, H. Tianyang, W. Mingxing, X. Fujun, W. Xinqiang, Y. Tongjun, F. Zheyu and S. Bo, *Superlattices Microstruct.*, 2017, **104**, 397–401.
20 U. Zeimer, J. Jeschke, A. Mogilatenko, A. Knauer, V. Kueller, V. Hoffmann, C. Kuhn, T. Simoneit, M. Martens, M. Wernicke, M. Kneissl and M. Weyers, *Semicond. Sci. Technol.*, 2015, **30**(11), 114008.
21 K. Gunnar, L. Haoning, R. E. Paul, B. Jochen, C. S. Thomas, J. P. Peter and W. M. Robert, *Appl. Phys. Lett.*, 2014, **104**(9), 092114.
22 A. Knauer, U. Zeimer, V. Kueller and M. Weyers, *Phys. Status Solidi C*, 2014, **11**(3–4), 377–380.

23 V. Kueller, A. Knauer, F. Brunner, A. Mogilatenko, M. Kneissl and M. Weyers, *Phys. Status Solidi C*, 2012, **9**(3–4), 496–498.
24 D. H. Lim, K. Xu, S. Arima and A. Yoshikawa, *J. Appl. Phys.*, 2002, **91**(10), 6461–6464.
25 S. J. Bak, D. H. Mun, K. C. Jung, J. H. Park, H. J. Bae, I. W. Lee, J.-S. Ha, T. Jeong and T. S. Oh, *Electron. Mater. Lett.*, 2013, **9**(3), 367–370.
26 Q. Bao, J. Luo and C. Zhao, *Vacuum*, 2014, **101**, 184–188.
27 C. Li, H. Liu and S. J. Chua, *J. Appl. Phys.*, 2015, **117**(12), 125305.
28 S. Haiding, W. Feng, J. P. Yong, T. M. Al Tahtamouni, L. Kuang-Hui, N. Alfaraj, T. Detchprohm, R. D. Dupuis and L. Xiaohang, *Appl. Phys. Lett.*, 2017, **110**(19), 192106.
29 S. Haiding, W. Feng, T. M. Al Tahtamouni, N. Alfaraj, L. Kuang-Hui, T. Detchprohm, R. D. Dupuis and L. Xiaohang, *J. Phys. D: Appl. Phys.*, 2017, **50**(39), 395101.
30 M. A. Moram and M. E. Vickers, *Rep. Prog. Phys.*, 2009, **72**(3), 036502.
31 K. N. Tu, J. W. Maye and L. C. Feldman, *Electronic Thin Film Science*, Macnillan College Publishing Company Inc, London, 1992, pp. 225–230.
32 A. R. Denton and N. W. Ashcroft, *Phys. Rev. A: At., Mol., Opt. Phys.*, 1991, **43**(6), 3161.
33 A. F. Wright, *J. Appl. Phys.*, 1997, **82**(6), 2833–2839.
34 N. Grandjean, J. Massies and M. Leroux, *Phys. Rev. B: Condens. Matter Mater. Phys.*, 1996, **53**(3), 998–1001.
35 S. Einfeldt, H. Heinke, V. Kirchner and D. Hommel, *J. Appl. Phys.*, 2001, **89**(4), 2160–2167.
36 D. Caceres, I. Vergara, R. Gonzalez, E. Monroy, F. Calle, E. Munoz and F. Omnes, *J. Appl. Phys.*, 1999, **86**(12), 6773–6778.
37 M. A. Moram, Z. H. Barber and C. J. Humphreys, *J. Appl. Phys.*, 2007, **102**(2), 023505.
38 H. J. Fitting, N. Cornet, R. Salh, C. Guerret-Piécourt, D. Goeuriot and A. V. Czarnowski, *J. Electron Spectrosc. Relat. Phenom.*, 2007, **159**(1–3), 46–52.
39 K. Kanaya and S. Okayama, *J. Phys. D: Appl. Phys.*, 1972, **5**(1), 43.
40 N. Nepal, M. L. Nakarmi, J. Y. Lin and H. X. Jiang, *Appl. Phys. Lett.*, 2006, **89**(9), 092107.
41 M. Nakarmi, N. Nepal, J. Y. Lin and H. X. Jiang, *Appl. Phys. Lett.*, 2009, **94**(9), 091903.
42 N. Nepal, J. Li, M. L. Nakarmi and H. X. Jiang, *Appl. Phys. Lett.*, 2006, **88**(6), 062103.
43 A. Bell, S. Srinivasan, C. Plumlee, H. Omiya and F. A. Ponce, *J. Appl. Phys.*, 2004, **95**(9), 4670–4674.
44 S. J. Chung, M. S. Kumar, H. J. Lee and E. K. Suh, *J. Appl. Phys.*, 2004, **95**(7), 3565–3568.
45 K. B. Lee, P. J. Parbrook, T. Wang and F. Ranalli, *J. Appl. Phys.*, 2007, **101**(5), 053513.
46 V. Yu. Davydov, Y. E. Kitaev, I. N. Goncharuk, A. Smirnov, J. Graul, O. Semchinova, D. Uffmann, M. B. Smirnov, A. P. Mirgorodsky and R. A. Evarestov, *Phys. Rev. B: Condens. Matter Mater. Phys.*, 1998, **58**(19), 12899.
47 T. Onuma, S. F. Chichibu, T. Sota, K. Asai, S. Sumiya, T. Shibata and M. Tanaka, *Appl. Phys. Lett.*, 2002, **81**(4), 652–654.